Salomäki, J. and Luomi, J. (2006). Vector control of an induction motor fed by a PWM inverter with output LC filter. European Power Electronics and Drives Association Journal, 16 (1), pp. 37-43.

Vector Control of an Induction Motor Fed by a PWM Inverter with Output LC Filter*

Janne Salomäki, Jorma Luomi, Helsinki University of Technology, Espoo, Finland

Keywords: Vector control, induction motor, LC filter, observer

Abstract

This paper introduces a control method for an induction motor that is supplied by a PWM voltage source inverter through an LC filter. A cascade control structure is employed and a full-order observer is used to estimate the system states. Thus no additional voltage or current measurements are needed for the vector control of the motor. Two alternative methods are presented for the observer gain selection. Simulation and experimental results confirm the functionality of the proposed control method.

Introduction

The voltage generated by a PWM frequency converter consists of sharp-edged voltage pulses. Sudden alterations of the voltage cause unwanted effects such as bearing currents and high voltage stresses in motor insulations. The oscillation at the switching frequency causes additional losses and acoustic noise. These phenomena can be reduced by adding an LC filter to the output of the PWM inverter. As the output voltage of the inverter is nearly sinusoidal, longer motor cables can be used, and the EMI shielding of the motor cable may be avoided. The use of an LC filter also introduces disadvantages. The size and the cost of the filter are not negligible, extra losses are dissipated in the filter, and acoustic noise can reappear in the filter itself. Moreover, the filter also causes an undesirable voltage drop. In many cases, however, adding an LC filter to an existing drive is considered necessary, or the advantages outweigh the disadvantages.

The control of an induction motor becomes more difficult if an LC filter is used. Usually, a very simple scalar control method (constant volts-per-hertz control) is chosen. Although better control performance is needed in many cases, only few publications deal with the vector control of an induction motor fed via an LC filter. A deadbeat controller has been used to control the inductor current and the capacitor voltage [1], the high-pass filtered stator voltage has been used to correct the voltage reference [2], and a multi-loop feedback controller has been proposed [3]. In these methods, extra current or voltage measurements are needed in addition to the phase current and dc-link voltage measurements usual in a frequency converter. For practical reasons, however, no additional hardware should be added to the frequency converter.

In this paper, a method is presented for the vector control of an induction motor fed by an inverter through an output LC filter. Cascaded controllers are used to control the inverter current, the stator voltage, the stator current and the rotor speed. The system states are estimated by a full-order observer. The method enables the motor control without any additional measurements.

Theory

The principle of the control system is shown in Fig. 1. Space vector notation is used for three-phase quantities. The inverter output voltage $\underline{u}_\mathrm{A}$ is filtered by an LC filter, and the induction motor (IM) is fed by the filtered voltage $\underline{u}_\mathrm{s}$. The inverter current $\underline{i}_\mathrm{A}$, the electrical angular speed ω_m of the rotor, and the dc-link voltage u_dc are the only measured quantities, whereas the stator voltage $\underline{u}_\mathrm{s}$ and current $\underline{i}_\mathrm{s}$ of the motor are estimated by an observer (the estimated quantities being marked by '^'). The system is controlled by cascaded controllers in the estimated rotor flux reference frame.

Filter and motor models

In a reference frame rotating at angular speed ω_s, the equations for the LC filter are

$$\frac{\mathrm{d}\underline{i}_\mathrm{A}}{\mathrm{d}t} = -\mathrm{j}\omega_\mathrm{s}\underline{i}_\mathrm{A} - \frac{R_\mathrm{Lf}}{L_\mathrm{f}}\underline{i}_A + \frac{1}{L_\mathrm{f}}(\underline{u}_\mathrm{A} - \underline{u}_\mathrm{s}) \tag{1}$$

$$\frac{\mathrm{d}\underline{u}_\mathrm{s}}{\mathrm{d}t} = -\mathrm{j}\omega_\mathrm{s}\underline{u}_\mathrm{s} + \frac{1}{C_\mathrm{f}}(\underline{i}_\mathrm{A} - \underline{i}_\mathrm{s}) \tag{2}$$

where L_f is the inductance and R_Lf the series resistance of the inductor, and C_f is the capacitance of the LC filter.

The inverse-Γ model [4] of the induction motor is used in the following. The stator and rotor voltage equations are

$$\underline{u}_\mathrm{s} = R_\mathrm{s}\underline{i}_\mathrm{s} + \frac{\mathrm{d}\underline{\psi}_\mathrm{s}}{\mathrm{d}t} + \mathrm{j}\omega_\mathrm{s}\underline{\psi}_\mathrm{s} \tag{3}$$

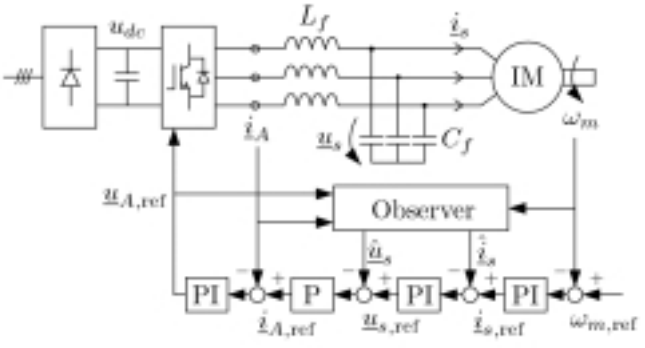

Fig. 1: Principle of the control system

* This paper has been designated as outstanding paper of NORPIE 2004

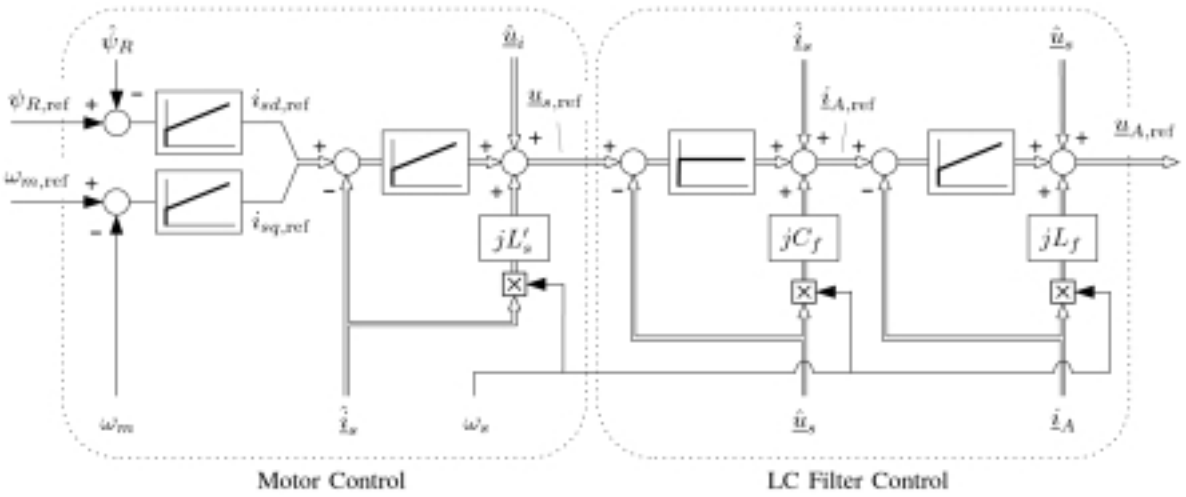

Fig. 2: Complex signal flow diagram of the cascade control

$$0 = R_{\mathrm{R}}\,\underline{i}_{\mathrm{R}} + \frac{\mathrm{d}\underline{\psi}_{\mathrm{R}}}{\mathrm{d}t} + \mathrm{j}(\omega_{\mathrm{s}} - \omega_{\mathrm{m}})\,\underline{\psi}_{\mathrm{R}} \tag{4}$$

respectively, where R_{s} and R_{R} are the stator and rotor resistances, respectively, $\underline{i}_{\mathrm{R}}$ is the rotor current, and ω_{m} is the electrical angular speed of the rotor. The stator and rotor flux linkages are

$$\underline{\psi}_{\mathrm{s}} = (L'_{\mathrm{s}} + L_{\mathrm{M}})\,\underline{i}_{\mathrm{s}} + L_{\mathrm{M}}\,\underline{i}_{\mathrm{R}} \tag{5}$$

$$\underline{\psi}_{\mathrm{R}} = L_{\mathrm{M}}(\underline{i}_{\mathrm{s}} + \underline{i}_{\mathrm{R}}) \tag{6}$$

respectively, where L'_{s} denotes the stator transient inductance and L_{M} is the magnetizing inductance. Based on (1)–(6), the state-space representation of the system can be written as

$$\dot{\mathbf{x}} = \underbrace{\begin{bmatrix} -\frac{R_{\mathrm{f}}}{L_{\mathrm{f}}} - \mathrm{j}\omega_{\mathrm{s}} & -\frac{1}{L_{\mathrm{f}}} & 0 & 0 \\ \frac{1}{C_{\mathrm{f}}} & -\mathrm{j}\omega_{\mathrm{s}} & -\frac{1}{C_{\mathrm{f}}} & 0 \\ 0 & \frac{1}{L'_{\mathrm{s}}} & -\frac{1}{\tau'_{\sigma}} - \mathrm{j}\omega_{\mathrm{s}} & \frac{1}{L'_{\mathrm{s}}}\left(\frac{1}{\tau_{\mathrm{r}}} - \mathrm{j}\omega_{\mathrm{m}}\right) \\ 0 & 0 & R_{\mathrm{R}} & -\frac{1}{\tau_{\mathrm{r}}} - \mathrm{j}(\omega_{\mathrm{s}} - \omega_{\mathrm{m}}) \end{bmatrix}}_{\mathbf{A}} \mathbf{x} + \underbrace{\begin{bmatrix} \frac{1}{L_{\mathrm{f}}} \\ 0 \\ 0 \\ 0 \end{bmatrix}}_{\mathbf{B}} \underline{u}_{\mathrm{A}} \tag{7}$$

$$\underline{i}_{\mathrm{A}} = \underbrace{\begin{bmatrix} 1 & 0 & 0 & 0 \end{bmatrix}}_{\mathbf{C}} \mathbf{x} \tag{8}$$

The state vector is $\mathbf{x} = [\underline{i}_{\mathrm{A}} \quad \underline{u}_{\mathrm{s}} \quad \underline{i}_{\mathrm{s}} \quad \underline{\psi}_{\mathrm{R}}]^{\mathrm{T}}$, and the two time constants are defined as: $\tau'_{\sigma} = L'_{\mathrm{s}}/(R_{\mathrm{s}} + R_{\mathrm{R}})$ and $\tau_{\mathrm{r}} = L_{\mathrm{M}} / R_{\mathrm{R}}$

Cascade control

Fig. 2 illustrates the proposed cascade control of the system in the estimated rotor flux reference frame. In the LC filter control, the innermost control loop governs the inverter current $\underline{i}_{\mathrm{A}}$ by means of a PI controller. In the next control loop, a *P* controller is sufficient for governing the stator voltage $\underline{u}_{\mathrm{s}}$ if the capacitor losses are low (and the capacitor can thus be considered as a pure integrator). In both control loops, the cross-couplings caused by the rotating reference frame are compensated.

The motor control forms the two outermost control loops. The stator current $\underline{i}_{\mathrm{s}}$ is controlled by a PI controller with cross-coupling and back-emf $\underline{u}_{\mathrm{i}}$ compensations, and the rotor speed ω_{m} is governed by a PI controller. In addition, a PI controller for the rotor flux is used.

Observability

The observability of the system can be investigated using the observability matrix

$$\mathbf{M}_{\mathrm{o}} = [\mathbf{C} \quad \mathbf{C}\underline{\mathbf{A}} \quad \mathbf{C}\underline{\mathbf{A}}^2 \quad \mathbf{C}\underline{\mathbf{A}}^3]^{\mathrm{T}} \tag{9}$$

The system is observable if the rank of the observability matrix is equal to the number of states [5]. The rank was checked numerically (for the example values used in the next sections) using the singular value decomposition algorithm included in the MATLAB software. The results indicated that the system is observable in the speed and slip region considered.

Full-order observer

The most essential part of the control is a full-order observer, which is implemented in the estimated rotor flux reference frame, i.e., in a reference frame where $\hat{\underline{\Psi}}_{\mathrm{R}} = \hat{\Psi}_{\mathrm{R}} + \mathrm{j}\theta$ The observer is defined as

$$\dot{\hat{\mathbf{x}}} = \underline{\mathbf{A}}\hat{\mathbf{x}} + \mathbf{B}\underline{u}_{\mathrm{A}} + \underline{\mathbf{K}}(\underline{i}_{\mathrm{A}} - \hat{\underline{i}}_{\mathrm{A}}) \tag{10}$$

where estimated states are marked by the symbol '^' and

$$\underline{\mathbf{K}} = [\underline{k}_1 \quad \underline{k}_2 \quad \underline{k}_3 \quad \underline{k}_4]^{\mathrm{T}}$$

is the observer gain. For the practical implementation of the observer, the estimated state vector is expressed in terms of the real and imaginary components (denoted by subscripts d and q, respectively) by writing

$$\hat{\mathbf{x}} = [\hat{i}_{\mathrm{Ad}} \quad \hat{i}_{\mathrm{Aq}} \quad \hat{u}_{\mathrm{sd}} \quad \hat{u}_{\mathrm{sq}} \quad \hat{i}_{\mathrm{sd}} \quad \hat{i}_{\mathrm{sq}} \quad \hat{\psi}_{\mathrm{Rd}} \quad \hat{\psi}_{\mathrm{Rq}}]^{\mathrm{T}}.$$

Correspondingly, $\mathbf{u}_{\mathrm{A}} = [u_{\mathrm{Ad}} \; u_{\mathrm{Aq}}]^{\mathrm{T}}$ is the inverter voltage and $\mathbf{i}_{\mathrm{A}} = [i_{\mathrm{Ad}} \; i_{\mathrm{Aq}}]^{\mathrm{T}}$ the inverter current in the component form. The system matrices **A** and **B** are now real-valued 8-by-8 and 8-by-2 matrices, respectively, and the gain matrix **K** is a real-valued 8-by-2 matrix.

The conventional forward Euler discretization is a simple discrete model of the full-order observer (10). It can be written as

$$\hat{\mathbf{x}}^{n+1} = \hat{\mathbf{x}}^{n} + T_{\mathrm{s}}\left[\mathbf{A}\hat{\mathbf{x}}^{n} + \mathbf{B}\mathbf{u}_{\mathrm{A}}^{n} + \mathbf{K}(\mathbf{i}_{\mathrm{A}}^{n} - \hat{\mathbf{i}}_{\mathrm{A}}^{n})\right] \tag{11}$$

where the sampling time is denoted by T_{s}, and the n^{th} time step by the superscript n. However, the digital implementation of the full-order observer based on the conventional forward Euler discretization causes instability at higher speeds. On the other hand, high-order discrete models are undesirable since they are more complicated to implement and require plenty of real-time calculation. A simple symmetric Euler method has been found to be an effective and reliable discretization method in electromechanical simulations [6] and full-order flux observers [7]. The corresponding discretization of the full-order observer (10) is given by

$$\hat{\mathbf{x}}^{n+1} = \hat{\mathbf{x}}^{n} + T_{\mathrm{s}}\left[\mathbf{A}_{\mathrm{U}}\hat{\mathbf{x}}^{n} + \mathbf{A}_{\mathrm{L}}\hat{\mathbf{x}}^{n+1} + \mathbf{B}\mathbf{u}_{\mathrm{A}}^{n} + \mathbf{K}(\mathbf{i}_{\mathrm{A}}^{n} - \hat{\mathbf{i}}_{\mathrm{A}}^{n})\right] \tag{12}$$

where $\mathbf{A}_{\mathrm{U}}$ is an upper triangular matrix including the corresponding entries of **A**, and $\mathbf{A}_{\mathrm{L}}$ is a lower triangular matrix including the corresponding entries of **A** but with zeroes on the diagonal. The detailed algorithm is given in the Appendix.

The observer gain $\underline{\mathbf{K}}$ affects the dynamic behavior of the observer. The gain selection can be based on the pole placement method, or a simple constant gain can be used, as will be presented in the following.

Pole placement

The dynamics of the estimation error $\tilde{\underline{\mathbf{x}}} = \underline{\mathbf{x}} - \hat{\underline{\mathbf{x}}}$ are given by

$$\dot{\tilde{\underline{\mathbf{x}}}} = (\underline{\mathbf{A}} - \underline{\mathbf{K}}\mathbf{C})\tilde{\underline{\mathbf{x}}} \tag{13}$$

In the pole placement method, the poles of the estimation error dynamics are placed to desired locations. Because the system model is time variant, the pole placement should be carried out at every calculation step. Gain scheduling can be used for avoiding excessive computing times: the observer gain is calculated in advance as a function of the angular speed of the rotor, and interpolation between tabulated values is used during the operation.

The poles also depend on the slip angular frequency $\omega_{\mathrm{r}} = \omega_{\mathrm{s}} - \omega_{\mathrm{m}}$ as the estimated rotor flux reference frame is used. If the gains obtained for no-load operation are used, the slip frequency affects only the imaginary parts of the observer poles, as illustrated in Fig. 3 for the example values used in the next sections. Therefore, the assumption of $\omega_{\mathrm{r}} = 0$ in the pole placement method is acceptable. After careful experimental analysis, the following pole locations were selected: (– 9.5 ± j9.5) p.u., – 2.7 p.u. and – 0.02 p.u. The

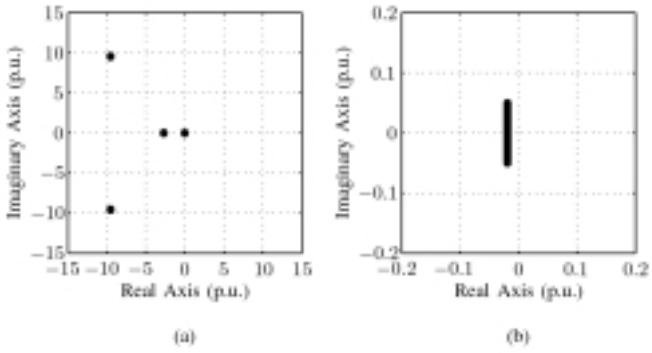

Fig. 3: Observer poles obtained by pole placement as rotor speed changes from – 1 to 1 p.u. and slip angular frequency changes from – 0.05 to 0.05 p.u.: (a) pole plot and (b) its magnification in the neighborhood of the origin.

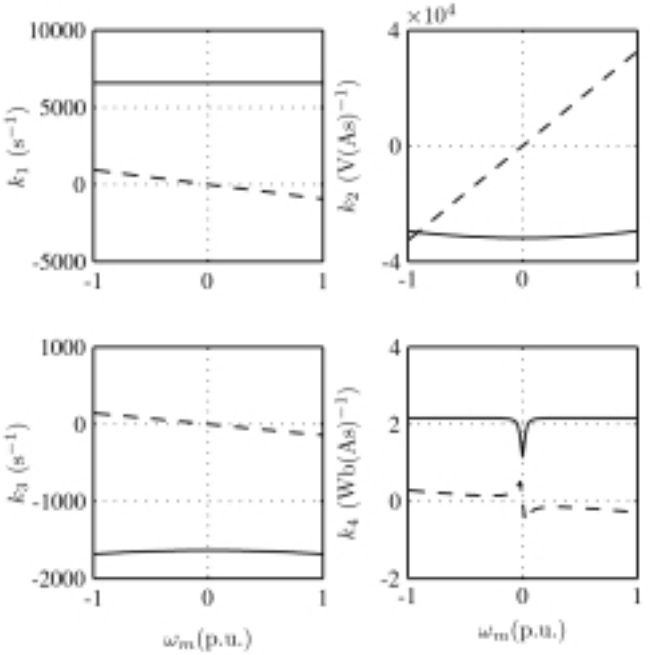

Fig. 4: Observer gain as function of rotor speed. The subplots show the real (solid) and imaginary (dashed) components of $\underline{k}_1$, $\underline{k}_2$, $\underline{k}_3$, and $\underline{k}_4$.

base value of the angular frequency is $2\pi \cdot 50$ rad/s. Fig. 4 shows the observer gain as a function of the rotor speed.

Simple constant gain

The observer becomes relatively simple when the real-valued gain $\underline{\mathbf{K}} = [k_1 \; 0 \; 0 \; 0]^{\mathrm{T}}$ is selected. By assuming that the estimated inverter current does not interact with the estimated stator voltage, the transfer function from the inverter current to its estimate can be written as

$$\frac{\hat{\underline{i}}_{\mathrm{A}}(s)}{\underline{i}_{\mathrm{A}}(s)} = \frac{k_1}{s + \dfrac{R_{\mathrm{Lf}}}{L_{\mathrm{f}}} + \mathrm{j}\omega_{\mathrm{s}} + k_1} \approx \frac{k_1}{s + k_1} \tag{14}$$

where the last approximation holds if $k_1 >> \left| R_{\mathrm{Lf}}/L_{\mathrm{f}} + \mathrm{j}\omega_{\mathrm{s}} \right|$. Thus the gain k_1 is approximately equal to the bandwidth of the inverter current estimation. It can be selected so that the estimation is at

least twice as fast as the controller of the inverter current. Fig. 5 illustrates the observer poles with $k_1 = 2\pi \cdot 1000\ s^{-1}$ as the speed and the slip of the motor are varied. The poles move more than those obtained by using the pole-placement method, but there is only a small variation in the real-axis direction. All poles stay in the left half-plane, indicating that the observer is stable.

Simulation results

The behavior of the system was investigated by means of computer simulations with the MATLAB/Simulink software. The frequency converter was modeled with a d.c. voltage source and an ideal three-phase inverter bridge. SimPowerSystems blocks were used for building the frequency converter model and the three-phase LC filter model. The induction motor model and the control algorithms were implemented with S-Functions in Simulink. Continuous models were used for the inverter, the LC-filter and the motor, whereas discrete-time models were used for the control algorithms. The solver algorithm was an implicit Runge-Kutta formula (TR-BDF2).

The data of a 2.2-kW four-pole induction motor (400 V, 50 Hz), given in Table I, were used for the simulations. The sampling frequency of 5 kHz was equal to the switching frequency. The LC filter was designed to have a resonance frequency of 566 Hz in order to meet a rule of thumb: the cutoff frequency should be about one decade below the switching frequency and one decade above the nominal fundamental frequency [8]. The fundamental-frequency voltage drop in the filter inductance was chosen to be less than 5 % of the nominal voltage in the nominal operating point [9]. The filter parameters are also given in Table I.

The bandwidths of the controllers are presented in Table II. The inverter current controller bandwidth α_{Ac} was selected to be one decade below the sampling frequency. It is the fast-est controller in the cascade control. The bandwidth α_v of the stator voltage controller was half of α_{Ac}, and the bandwidth α_c of the stator current controller was approximately half of α_v. The speed controller bandwidth α_s was selected to be one decade below α_c. The flux controller was selected to be the slowest controller with the bandwidth of $\alpha_f = 0.2 \cdot \alpha_s$. In the field weakening region, the flux controller bandwidth was increased in order to change the flux more rapidly.

The observer gain values were obtained by using gain scheduling as explained in the previous section. The reference value of the inverter voltage $\underline{u}_{A,ref}$ was used in the observer to avoid the switching ripple and the filtering of the measured inverter voltage $\underline{u}_A$. The time delay of 1.5 T_s from the sampling time to the weight center of the PWM cycle was compensated.

Fig. 6 shows an example of simulated sequences, consisting of accelerations, nominal load torque steps at various speeds, and a deceleration ramp to standstill. The results show that the operation of the system is successful. The rotor speed is in accordance with its reference, and the torque behaves as expected. The rotor flux linkage is reduced by 15 % at the highest speed because of field weakening.

Fig. 7 shows a magnification of the results around the first speed reference step in Fig. 6. The rotor speed increases fast and smoothly, and only a small overshoot occurs. The dynamic behavior of the currents is also satisfactory. The q components of the inverter and stator currents are nearly equal, but the d components differ from each other at higher speeds because a part of the magnetizing current of the motor is fed by the filter capacitor. The voltage and current wave-forms are illustrated in detail in Fig. 8. The stator voltage and current are nearly sinusoidal.

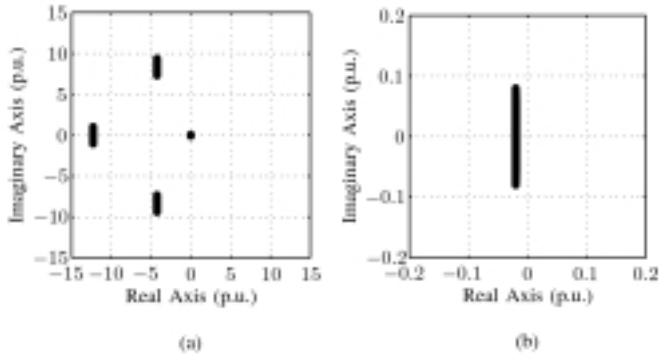

Fig. 5: Observer poles obtained by constant gain as rotor speed changes from – 1 to 1 p.u. and slip angular frequency changes from – 0.05 to 0.05 p.u.: (a) pole plot and (b) its magnification in the neighborhood of the origin.

Table I: Parameters of the motor and the LC filter

Motor Parameters	
Stator resistance R_s	3.67 Ω
Rotor resistance R_r	1.65 Ω
Stator transient inductance L'_s	0.0209 H
Magnetizing inductance L_M	0.264 H
Total moment of inertia J	0.0155 kgm^2
Rated speed n_N	1430 r/min
Rated current I_N	5.0 A
Rated torque T_N	14.6 Nm
LC Filter Parameters	
Inductance L_f	8.0 mH
Capacitance C_f	9.9 μF
Series resistance R_{Lf}	0.1 Ω

Table II: Bandwidths of the controllers

Inverter current controller α_{Ac}	$2\pi \cdot 500$ rad/s
Stator voltage controller α_v	$2\pi \cdot 250$ rad/s
Stator current controller α_c	$2\pi \cdot 150$ rad/s
Speed controller α_s	$2\pi \cdot 15$ rad/s
Flux controller α_f	$2\pi \cdot 3$ rad/s
Flux controller in field weakening α_{fw}	$2\pi \cdot 15$ rad/s

Experimental results

The experimental setup is illustrated in Fig. 9. The 2.2-kW four-pole induction motor was fed by a frequency converter controlled by a dSPACE DS1103 PPC/DSP board. The control system was based on the Simulink model used for the control in the simulations. In the experimental setup, simple current feedforward compensation for dead times and power device voltage drops [10] was added to the control system, and the measured saturation characteristic, depicted in Fig. 10, was used for the magnetizing inductance. Three 3.3-μF filter capacitors were used in delta connection, giving the per-phase capacitance value of 9.9 μF. The measured dc-link voltage, phase currents and rotor speed were used as feedback signals for the control. The shaft torque was measured using a HBM T10F torque flange for monitoring purposes. A permanent magnet servo motor was used to provide load torque.

Fig. 11(a) presents experimental results corresponding to the simulations shown in Fig. 6. The measured performance corresponds

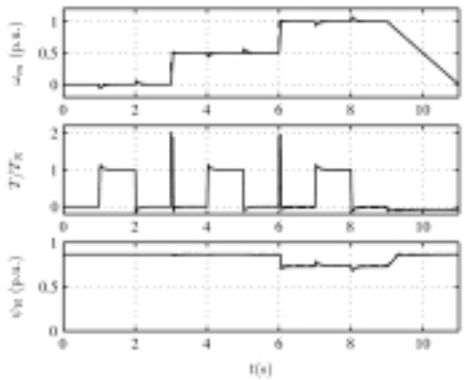

Fig. 6: Simulation results showing a sequence with speed and load changes. The first subplot shows the rotor speed (solid) and its reference (dashed). The second subplot shows the electromagnetic torque (solid) and its reference (dashed) normalized by the rated torque T_N. The third subplot shows the rotor flux linkage (solid) and its estimate (dashed).

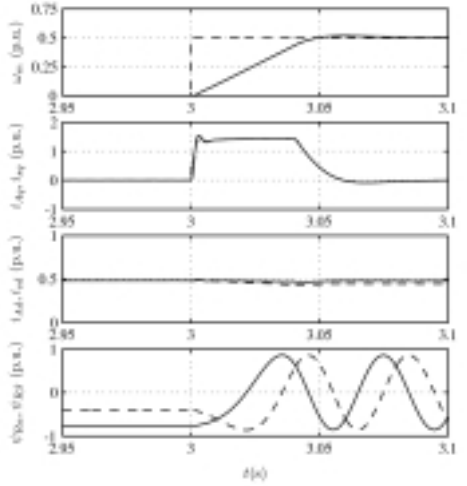

Fig. 7: Simulation results showing a magnification of the results around the first speed reference step in Fig. 6. The first subplot shows the rotor speed (solid) and its reference (dashed). The second subplot shows the q components of the stator (solid) and inverter (dashed) currents. The third subplot shows the d components of the stator (solid) and inverter (dashed) currents. The fourth subplot shows the rotor flux components in the stator reference frame.

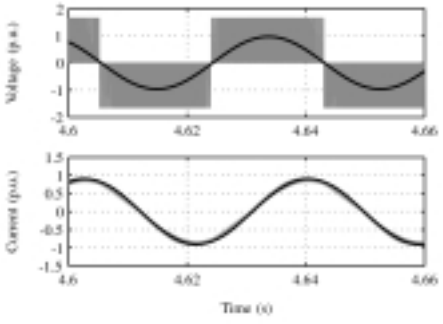

Fig. 8: Voltage and current waveforms from the simulation shown in Fig. 6. The first subplot shows the inverter output voltage (phase-to-phase) and the stator voltage (phase-to-phase). The second subplot shows the inverter current and the stator current.

to the simulation results rather well. The total moment of inertia of the setup was 2.2 times the inertia of the induction motor, which causes a large part of the difference between the measured shaft torque and the electromagnetic torque reference during the accelerations. During transients, the estimated rotor flux deviates slightly from the reference. Experiments were also carried out using the observer with the constant gain of $k_1 = 2\pi \cdot 1000\ s^{-1}$. The results, shown in Fig. 11(b), are similar to those obtained by using the pole placement method.

Fig. 12 shows a magnification of the results around the first speed reference step in Fig. 11. The acceleration is fast, and the overshoot is very small with both gain selection methods. The q components of the stator and inverter currents have a small overshoot after the speed reference step. The oscillation of the currents is slightly larger in the case of the constant gain, but the performance is very similar to that of the more complicated observer. It seems to be reasonable to use a constant gain in the observer instead of the pole placement method. The measured voltage and current waveforms are illustrated in detail in Fig. 13. These results are in good agreement with the simulation results.

Conclusions

When the inverter output voltage is filtered by an LC filter, the vector control of an induction motor can be based on cascaded control loops. The system states can be estimated by a full-order observer, requiring only the measurements of inverter current, dc-link voltage, and rotor speed. Because no additional measurements are needed, the control method enables an LC filter to be used in a standard frequency converter drive; only changes in the software are required. Simulation and experimental results show that the proposed control method works correctly. The observer gain can be selected by means of pole placement, but a constant gain gives similar results and is easier to use.

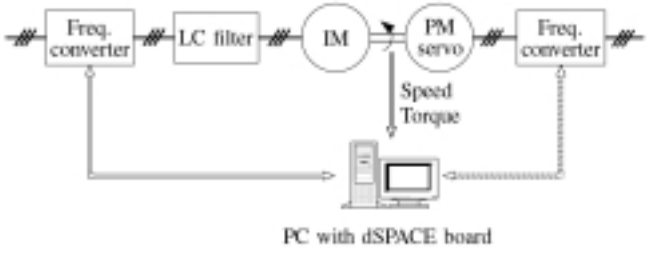

Fig. 9: Experimental setup. Control of induction motor (IM) is investigated, and permanent magnet (PM) servo motor is used as loading machine. Measured shaft torque is used only for monitoring.

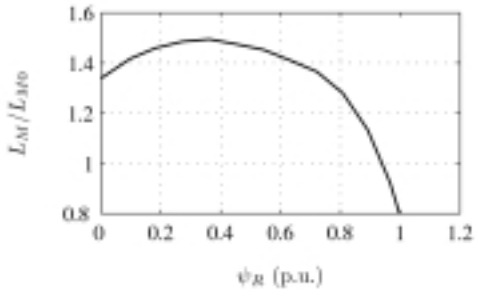

Fig. 10: Measured magnetizing inductance of the 2.2-kW motor. Base value of the flux is 1.04 Wb and L_{M0} = 0.224 H

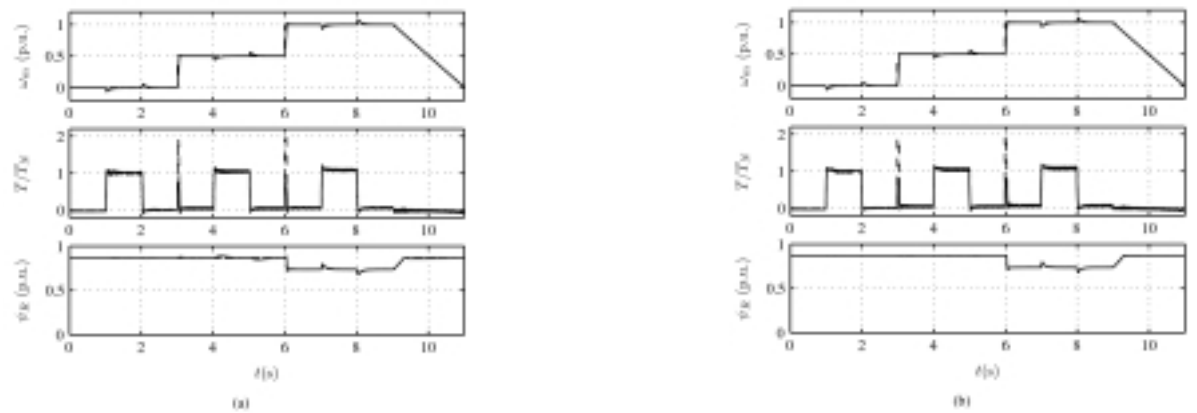

Fig. 11: Experimental results showing a sequence with speed and load changes as (a) observer gain is obtained by pole placement, and (b) observer gain is constant. The first subplot shows the rotor speed (solid) and its reference (dashed). The second subplot shows the measured shaft torque (solid) and the electromagnetic torque reference (dashed). The third subplot shows the rotor flux reference (dashed) and the estimated rotor flux (solid).

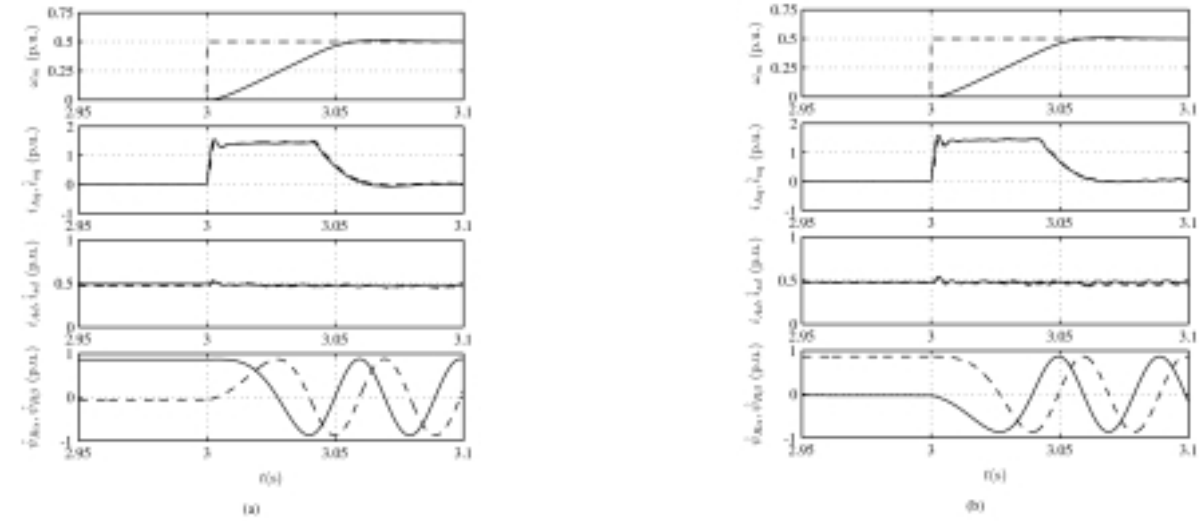

Fig. 12: Magnification of experimental results around the first speed reference step in Fig. 11 as (a) observer gain is obtained by pole placement, and (b) observer gain is constant. The first subplot shows the rotor speed (solid) and its reference (dashed). The second subplot shows the q components of the stator (solid) and inverter (dashed) currents. The third subplot shows the d components of the stator (solid) and inverter (dashed) currents. The fourth subplot shows the rotor flux components in the stator reference frame.

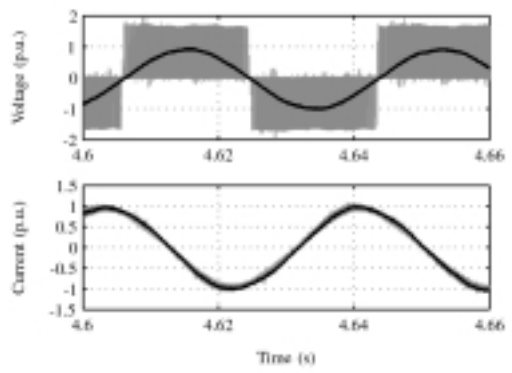

Fig. 13: Experimental result showing voltage and current waveforms as the rotational speed is 0.5 p.u. and the load torque is 14.6 Nm. The first subplot shows the inverter output voltage (phase-to-phase) and the stator voltage (phase-to-phase). The second subplot shows the inverter current and the stator current.

Acknowledgments

The authors wish to thank the reviewers for their insightful comments and helpful suggestions aimed at improving the paper. The financial support given by ABB Oy is gratefully acknowledged.

References

[1] M. Kojima, K. Hirabayashi, Y. Kawabata, E.C. Ejiogu, and T. Kawabata: Novel vector control system using deadbeat controlled PWM inverter with output LC filter, in Conf. Rec. IEEE/IAS Annu. Meeting, vol. 3, Pitts-burgh, PA, Oct. 2002, pp. 2102-2109.

[2] A. Nabae, H. Nakano, and Y. Okamura: A novel control strategy of the inverter with sinusoidal voltage and current outputs, in Proc. IEEE PESC'94, vol. 1, Taipei, Taiwan, June 1994, pp. 154-159.

[3] R. Seliga and W. Koczara: Multiloop feedback control strategy in sine-wave voltage inverter for an adjustable speed cage induction motor drive system, in Proc. EPE 2001, Graz, Austria, Aug. 2001, CD-ROM.

[4] G.R. Slemon: Modelling of induction machines for electric drives, IEEE Trans. Ind. Applicat., vol. 25, Nov./Dec. 1989, pp. 1126-1131.

[5] G.F. Franklin, J. D. Powell, and A. Emami-Naeini, Feedback Control of Dynamic Systems, 4th ed., Prentice Hall, Upper Saddle River, NJ, 2002.

[6] J. Niiranen: Fast and accurate symmetric Euler algorithm for electro-mechanical simulations, in Proc. Electrimacs'99, Lisboa, Portugal, Sept. 1999, pp. 71-78.

[7] M. Hinkkanen and J. Luomi: Parameter sensitivity of full-order flux observers for induction motors, IEEE Trans. Ind. Applicat. vol. 39, July/Aug. 2003, pp. 1127-1135.

[8] J. Steinke, C. Stulz, and P. Pohjalainen: Use of a LC filter to achieve a motor friendly performance of the PWM voltage source inverter, in Proc. IEEE IEMDC'97, Milwaukee, WI, May 1997, pp. TA2/4.1-TA2/4.3.

[9] C. Xiyou, Y. Bin, and G. Yu: The engineering design and the optimization of inverter output RLC filter in AC motor drive system, in Proc. IEEE IECON'02, vol. 1, Sevilla, Spain, Nov. 2002, pp. 175-180.

[10] J. K. Pedersen, F. Blaabjerg, J. W. Jensen, and P. Thøgersen: An ideal PWM-VSI inverter with feedforward and feedback compensation, in Proc. EPE'93, vol. 4, Brighton, U.K., Sept. 1993, pp. 312-318.

Appendix: Digital Implementation

The full-order observer (10) is discretized using the symmetric Euler method [6]. In contrast to the forward Euler method, the new state values are used when available. The discretized observer is given by

$$\hat{i}_{\mathrm{Ad}}^{\mathrm{n}+1} = \hat{i}_{\mathrm{Ad}}^{\mathrm{n}} + T_{\mathrm{s}}\left[-\frac{R_{\mathrm{Lf}}}{L_{\mathrm{f}}}\hat{i}_{\mathrm{Ad}}^{\mathrm{n}} + \hat{\omega}_{\mathrm{s}}^{\mathrm{n}}\hat{i}_{\mathrm{Aq}}^{\mathrm{n}} - \frac{1}{L_{\mathrm{f}}}\hat{u}_{\mathrm{sd}}^{\mathrm{n}} + \frac{1}{L_{\mathrm{f}}}u_{\mathrm{Ad}}^{\mathrm{n}} + k_{1\mathrm{d}}\tilde{i}_{\mathrm{Ad}}^{\mathrm{n}} - k_{1\mathrm{q}}\tilde{i}_{\mathrm{Aq}}^{\mathrm{n}}\right] \tag{15a}$$

$$\hat{i}_{\mathrm{Aq}}^{\mathrm{n}+1} = \hat{i}_{\mathrm{Aq}}^{\mathrm{n}} + T_{\mathrm{s}}\left[-\frac{R_{\mathrm{Lf}}}{L_{\mathrm{f}}}\hat{i}_{\mathrm{Aq}}^{\mathrm{n}} - \hat{\omega}_{\mathrm{s}}^{\mathrm{n}}\hat{i}_{\mathrm{Ad}}^{\mathrm{n}+1} - \frac{1}{L_{\mathrm{f}}}\hat{u}_{\mathrm{sq}}^{\mathrm{n}} + \frac{1}{L_{\mathrm{f}}}u_{\mathrm{Aq}}^{\mathrm{n}} + k_{1\mathrm{q}}\tilde{i}_{\mathrm{Ad}}^{\mathrm{n}} + k_{1\mathrm{d}}\tilde{i}_{\mathrm{Aq}}^{\mathrm{n}}\right] \tag{15b}$$

$$\hat{u}_{\mathrm{sd}}^{\mathrm{n}+1} = \hat{u}_{\mathrm{sd}}^{\mathrm{n}} + T_{\mathrm{s}}\left[\frac{1}{C_{\mathrm{f}}}\hat{i}_{\mathrm{Ad}}^{\mathrm{n}+1} + \hat{\omega}_{\mathrm{s}}^{\mathrm{n}}\hat{u}_{\mathrm{sq}}^{\mathrm{n}} - \frac{1}{C_{\mathrm{f}}}\hat{i}_{\mathrm{sd}}^{\mathrm{n}} + k_{2\mathrm{d}}\tilde{i}_{\mathrm{Ad}}^{\mathrm{n}} - k_{2\mathrm{q}}\tilde{i}_{\mathrm{Aq}}^{\mathrm{n}}\right] \tag{15c}$$

$$\hat{u}_{\mathrm{sq}}^{\mathrm{n}+1} = \hat{u}_{\mathrm{sq}}^{\mathrm{n}} + T_{\mathrm{s}}\left[\frac{1}{C_{\mathrm{f}}}\hat{i}_{\mathrm{Aq}}^{\mathrm{n}+1} - \hat{\omega}_{\mathrm{s}}^{\mathrm{n}}\hat{u}_{\mathrm{sd}}^{\mathrm{n}+1} - \frac{1}{C_{\mathrm{f}}}\hat{i}_{\mathrm{sq}}^{\mathrm{n}} + k_{2\mathrm{q}}\tilde{i}_{\mathrm{Ad}}^{\mathrm{n}} + k_{2\mathrm{d}}\tilde{i}_{\mathrm{Aq}}^{\mathrm{n}}\right] \tag{15d}$$

$$\hat{i}_{\mathrm{sd}}^{\mathrm{n}+1} = \hat{i}_{\mathrm{sd}}^{\mathrm{n}} + T_{\mathrm{s}}\left[\frac{1}{L_{\mathrm{s}}'}\hat{u}_{\mathrm{sd}}^{\mathrm{n}+1} - \frac{1}{\tau_{\sigma}'}\hat{i}_{\mathrm{sd}}^{\mathrm{n}} + \hat{\omega}_{\mathrm{s}}^{\mathrm{n}}\hat{i}_{\mathrm{sq}}^{\mathrm{n}} + \frac{1}{L_{\mathrm{s}}'\tau_{\mathrm{r}}}\hat{\psi}_{\mathrm{R}}^{\mathrm{n}} + k_{3\mathrm{d}}\tilde{i}_{\mathrm{Ad}}^{\mathrm{n}} - k_{3\mathrm{q}}\tilde{i}_{\mathrm{Aq}}^{\mathrm{n}}\right] \tag{15e}$$

$$\hat{i}_{\mathrm{sq}}^{\mathrm{n}+1} = \hat{i}_{\mathrm{sq}}^{\mathrm{n}} + T_{\mathrm{s}}\left[\frac{1}{L_{\mathrm{s}}'}\hat{u}_{\mathrm{sq}}^{\mathrm{n}+1} - \frac{1}{\tau_{\sigma}'}\hat{i}_{\mathrm{sq}}^{\mathrm{n}} - \hat{\omega}_{\mathrm{s}}^{\mathrm{n}}\hat{i}_{\mathrm{sd}}^{\mathrm{n}+1} - \frac{\omega_{\mathrm{m}}^{\mathrm{n}}}{L_{\mathrm{s}}'}\hat{\psi}_{\mathrm{R}}^{\mathrm{n}} + k_{3\mathrm{q}}\tilde{i}_{\mathrm{Ad}}^{\mathrm{n}} + k_{3\mathrm{d}}\tilde{i}_{\mathrm{Aq}}^{\mathrm{n}}\right] \tag{15f}$$

$$\hat{\psi}_{\mathrm{R}}^{\mathrm{n}+1} = \hat{\psi}_{\mathrm{R}}^{\mathrm{n}} + T_{\mathrm{s}}\left[R_R\hat{i}_{\mathrm{sd}}^{\mathrm{n}+1} - \frac{1}{\tau_{\mathrm{r}}}\hat{\psi}_{\mathrm{R}}^{\mathrm{n}} + k_{4\mathrm{d}}\tilde{i}_{\mathrm{Ad}}^{\mathrm{n}} - k_{4\mathrm{q}}\tilde{i}_{\mathrm{Aq}}^{\mathrm{n}}\right] \tag{15g}$$

$$\hat{\omega}_{\mathrm{s}}^{\mathrm{n}+1} = \frac{\hat{i}_{\mathrm{sq}}^{\mathrm{n}+1}R_{\mathrm{R}} + k_{4\mathrm{q}}\tilde{i}_{\mathrm{Ad}}^{\mathrm{n}} + k_{4\mathrm{d}}\tilde{i}_{\mathrm{Aq}}^{\mathrm{n}}}{\hat{\psi}_{\mathrm{R}}^{\mathrm{n}+1}} + \omega_{\mathrm{m}}^{\mathrm{n}} \tag{15h}$$

The Authors

Janne Salomäki was born in Hyvinkää, Finland, in 1978. He received his M.Sc. (Eng.) degree from Helsinki University of Technology, Espoo, Finland, in 2003. Since 2003, he has worked as a Researcher at the Power Electronics Laboratory, Helsinki University of Technology. His main research interest is the control of electrical drives.

Jorma Luomi received the M.Sc. (Eng.) and D.Sc. (Tech.) degrees from Helsinki University of Technology, Espoo, Finland, in 1977 and 1984, respectively. In 1980, he joined Helsinki University of Technology, and from 1991 to 1998 he was a Professor at Chalmers University of Technology. Since 1998, he has been a Professor in the Department of Electrical and Communications Engineering, Helsinki University of Technology. His research interests are in the areas of electric drives, electric machines, and numerical analysis of electromagnetic fields.